Inorganic Chemistry

Article

pubs.acs.org/IC

Crystal Structure, Electronic Structure, and Optical and Photoluminescence Properties of Eu(III) Ion-Doped $Lu_6Mo(W)O_{12}$

Huaiyong Li,[†] Hyun Kyoung Yang,[†] Byung Kee Moon,[†] Byung Chun Choi,[†] Jung Hyun Jeong,*[,†] Kiwan Jang,[‡] Ho Sueb Lee,[‡] and Soung Soo Yi[§]

[†]Department of Physics, Pukyong National University, Busan 608-737, Republic of Korea

[‡]Department of Physics, Changwon National University, Changwon 641-773, Republic of Korea

[§]Department of Electronic Material Engineering, Silla University, Busan 617-736, Republic of Korea

Supporting Information

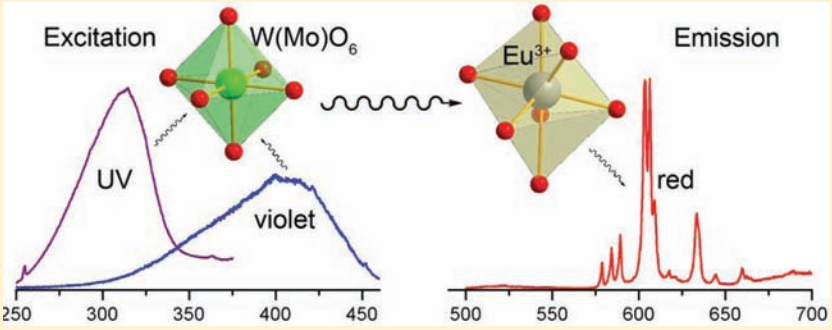

ABSTRACT: Lu_6WO_{12} and Lu_6MoO_{12} doped with Eu^{3+} ions have been prepared by using a citrate complexation route, followed by calcination at different temperatures. The morphology, structure, and optical and photoluminescence properties of the compounds were studied as a function of calcination temperature. Both compositions undergo transitions from a cubic to a hexagonal phase when the calcination temperature increases. All the compositions have strong absorption of near-UV light and show intense red luminescence under a near-UV excitation, which is related to the transfer of energy from the host lattices to dopant Eu^{3+} ions. Density functional theory calculations have also been performed. The calculation reveals that hexagonal Lu_6WO_{12} and Lu_6MoO_{12} are indirect bandgap materials, and the near-UV excitations are due to the electronic transitions from the O-2p orbitals to W-5d and Mo-4d orbitals, respectively. The lattice parameters and bandgap energies of hexagonal Lu_6WO_{12} and Lu_6MoO_{12} were determined.

1. INTRODUCTION

Inorganic tungstates and molybdates have attracted a great amount of interest because of their significant technological importance and novel structure−property relationship. They have been widely used as high-performance luminescent materials,[1−13] catalysts,[14−23] oxide ion- and proton-conducting materials,[24−29] and other functional materials on the basis of their promising optical, electronic, thermal, and chemical properties. In terms of the composition and structure, because a large amount of binary and ternary oxides can be combined from WO_3/MoO_3 and other oxides with general formulae of $M^{III}_2O_3$, $M^{II}O$, and M^{I}_2O, the crystal chemistry of inorganic tungstates and molybdates is widely extended. Among these compounds, rare earth tungstates and molybdates with an R_6MO_{12} composition (R, rare earth elements; M, W or Mo) have been investigated for decades, and the major concerns were the synthesis, structural identifying, and crystal chemistry. According to the literature, the structure of these compounds depends on the M/R radius ratio.[30] The tungstates crystallize in a cubic or pseudocubic phase from La to Pr,[31−33] a pseudotetragonal phase from Nd to Gd,[32−35] and a hexagonal phase from Tb to Lu, plus Y.[30,33,36] It was also reported that Y_6WO_{12} undergoes a transition in structure from the hexagonal phase to a metastable cubic phase at 1765 °C.[36,37] In the case of the molybdates, form La to Dy, it is cubic;[33] from Er to Lu, and Y, it is hexagonal,[30,33] and Ho adopts both cubic and hexagonal phases.[30,33] In recent years, renewed interest in these compounds has arisen. La_6WO_{12},[38−44] Nd_6WO_{12},[41,43] Eu_6WO_{12}, and Er_6WO_{12} were studied as proton−electron conductive materials for electrolytes of high-temperature solid oxide fuel cells or membranes of hydrogen separation.[41,43,45] Y_6WO_{12},[46−48] Gd_6WO_{12}, and Y_6MoO_{12} were thought to be hosts as well as sensitizers of Eu^{3+} ions,[48−50] which can be used as color-conversion phosphor for a white light-emitting diode (WLED). The optical properties of Y_6WO_{12} and its solid solutions with CeO_2 and Y_6MoO_{12} have also been studied.[51,52] Although the structural transition and the structure−property relationship attracted attention, the specific structural parameters of these compounds are still lacking, and only those of

Received: July 8, 2011
Published: November 21, 2011

 © 2011 American Chemical Society

La_6WO_{12}, Y_6WO_{12}, and Ho_6WO_{12} have been reported.[38,46,53] Systematic investigation on the structure−property relationship has seldom been reported.[43,46−48,51,52]

In this Article, we report a theoretical and experimental investigation of the synthesis and properties of Eu^{3+} ion-activated Lu_6WO_{12} (LWO) and Lu_6MoO_{12} (LMO) compounds. The samples have been synthesized on the basis of a citrate complexation route. The morphology, structure, and optical and photoluminescence properties of the samples have been characterized. As is well-known, the properties of materials are closely related to the chemical composition, crystal structure, and electronic structure. Density functional theory (DFT) calculations have also been performed because they can offer us detailed information about the arrangement of atoms and orbits and help us understand the structure−property relationship. It was found that the properties of the compounds varied systematically with the crystal structure and the crystallinity. All samples show strong absorption of near-UV light and red luminescence under near-UV excitation, which contributed to the transfer of energy from host lattices to dopant Eu^{3+} ions.

2. EXPERIMENTAL SECTION

2.1. Materials and Synthesis. The starting materials, Lu_2O_3 (99.9%), Eu_2O_3 (99.99%), $(NH_4)_6Mo_7O_{24}\cdot 4H_2O$ (99.98%), $(NH_4)_{10}H_2(W_2O_7)_6$ (99.99%), and citric acid $C_6H_8O_7$ (>99.5%), were obtained from Sigma-Aldrich and used as received. Powder samples were prepared by using a citrate complexation method, followed by calcination at different temperatures. In a typical synthesis procedure for 2.5 mol % Eu^{3+} ion-doped LWO, Lu_2O_3 (5.850 mmol) and Eu_2O_3 (0.150 mmol) were dissolved in hot diluted HNO_3 under vigorous stirring to form solution A, the pH value of which was adjusted to 2−3 with dilute $NH_3\cdot H_2O$, and then citric acid (12.0 mmol) was added to solution A to form a complex with the metal ions. Solution B was prepared by dissolving $(NH_4)_{10}H_2(W_2O_7)_6$ (0.167 mmol) in distilled water, and then the metal ion was complexed with citric acid (24.0 mmol). Solutions A and B were mixed together, magnetically stirred for 30 min, and then bathed in water at 70 °C until a porous gel formed. The gel was first heated at 200 °C for 4 h and then precalcined at 700 °C for 4 h. After being finely ground, the powder was divided into six batches and calcined in the range of 800−1300 °C with an interval of 100 °C for 4 h in air to produce the final products. LWO:Eu-*T* and LMO:Eu-*T* hereafter stand for LWO:Eu and LMO:Eu samples calcined at temperature *T*, respectively.

2.2. Characterization. The morphology of the polycrystalline samples was checked with a JSM-6700F (JEOL) field emission scanning electron microscope (FE-SEM) at 15 kV. The compositional analysis was determined by energy dispersive X-ray spectroscopy (EDX) on the JSM-6700F FE-SEM. Powder X-ray diffraction (XRD) measurements were taken on a D/MAX 2500 instrument (Rigaku) with a Rint 2000 wide angle goniometer and Cu Kα_1 radiation (λ = 1.54056 Å) at 40 kV and 100 mA. The diffraction patterns were scanned over an angular (2θ) range of 20−80° at intervals of 0.02° with a counting time of 0.6 s per step. UV−vis diffuse reflectance (DR) spectra were recorded on a V-670 (JASCO) UV−vis spectrophotometer. Photoluminescence (PL) studies were conducted on a fluorescence spectrophotometer (Photon Technology International) equipped with a 60 W Xe-arc lamp as the excitation light source. The temporal decay of the PL was measured with a phosphorimeter attached to the fluorescence spectrophotometer. All the measurements were taken at room temperature.

2.3. Details of the Calculation. DFT calculations on hexagonal LWO and LMO were conducted by using CASTEP code.[54] Geometry optimization and calculation of properties were performed to determine the crystal structure, electronic structure, and orbital population. For both compounds, the Vanderbilt ultrasoft pseudopotential[55] with a cutoff energy of 390 eV was used, and k-points of 3 × 3 × 4 were generated by using the Monkhorst−Pack scheme.[56] The exchange and correlation functionals were treated by the local density approximation (LDA) in the formulation of CA-PZ.[57,58] During the geometry optimization, lattice parameters and atomic positions were optimized simultaneously. For the self-consistent field iterations, the convergence tolerance for geometry optimization was selected with the differences in total energy, the maximal ionic Hellmann−Feynman force, the stress tensor, and the maximal displacement being within 5.0 × 10^{-6} eV/atom, 1.0 × 10^{-2} eV/Å, 2.0 × 10^{-2} GPa, and 5.0 × 10^{-4} Å, respectively.

3. RESULTS AND DISCUSSION

3.1. Morphological and Constituent Analysis. Figure 1 depicts the SEM microimages and constituent element data from EDX analysis of LMO:Eu samples calcined at different temperatures. The SEM microimages show that the samples are an agglomeration of irregular particles. This is due to the synthesis procedure, citrate complexation precursor, and high-temperature calcination, and therefore, totally separated particles are hard to form. From the indistinct particle boundary, the particle sizes can be approximately estimated to be in the range of 100−500 nm. From the variation of morphology and size, it also can be deduced that the samples go through a contraction−sinter−crystallization−growth process. The EDX data confirm the presence of Lu, Eu, Mo, and O in the obtained samples, and the (Lu+Eu):Mo:O constituent ratio is 32.36:5.16:62.38, which agrees with the theoretical ratio of 6:1:12. The related results for LWO:Eu samples are shown in Figure S1 of the Supporting Information. The morphology and particle size of LWO:Eu samples are similar to those of LMO:Eu samples except LWO:Eu samples are better sintered. All the elements are presented in the EDX data, and the ratio is consistent with the theoretical value.

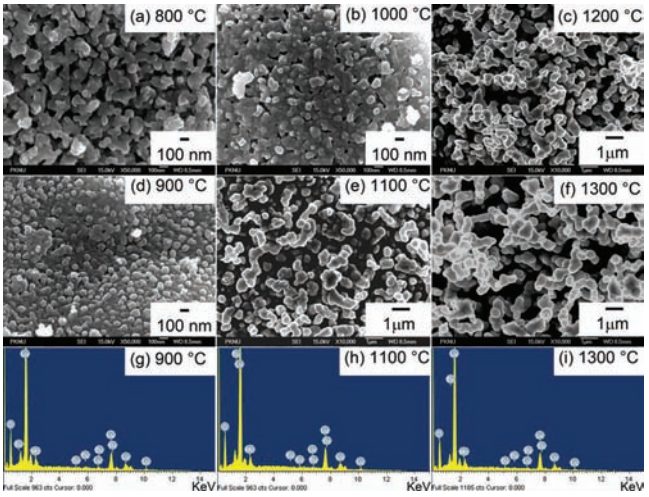

Figure 1. SEM microimages and EDX data of LMO:Eu samples calcined at different temperatures: (a) 800, (b) 1000, (c) 1200, (d and g) 900, (e and h) 1100, and (f and i) 1300 °C.

3.2. Structure Refinement and Cell Parameters. The XRD patterns of LWO:Eu and LMO:Eu calcined at different temperatures are shown in Figure 2. It is revealed that both compounds could crystallize into a cubic and a hexagonal structure depending on the calcination temperature. The hexagonal structure could be obtained at a calcination temperature higher than 1200 °C. The diffraction peaks of the hexagonal phase agree well with those recorded on JCPDS

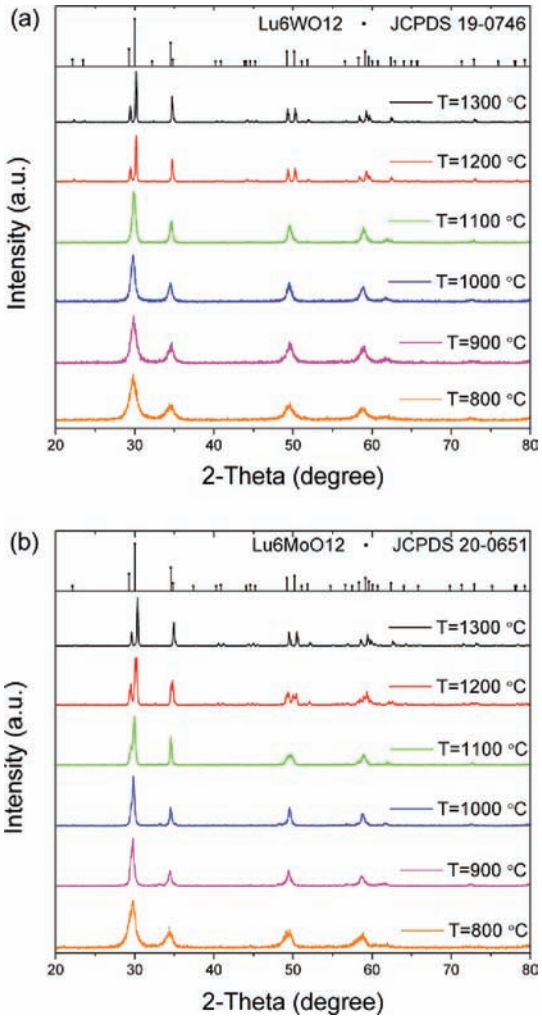

Figure 2. XRD patterns of (a) LWO:Eu and (b) LMO:Eu as a function of the final calcination temperature *T*.

cards 20-0651 and 19-0746. Cubic phase LWO:Eu and LMO:Eu existed in a temperature range of 800−1100 °C. The diffraction peaks of the cubic phase are similar to those of some other reported R_6WO_{12} compounds within a defect fluorite structure.[59] In the structure, a disorder arrangement of R^{3+} and M^{6+} ions was suggested, even though there is great difference in radius. The XRD patterns evolve systematically with the calcination temperature. A decrease in the calcination temperature results in broad and weak diffraction peaks, which indicates that the crystallinity of the samples decreases, and the long-range disorder increases. From the known hexagonal R_6MO_{12} compounds, Aitken et al. concluded that the stability of these compounds depended on the M/R radius ratio.[30] We suggest that there might be some relationships between the stability of the compounds and their cubic−hexagonal transition temperature. As reported, the hexagonal Er_6WO_{12} forms at a temperature higher than 1300 °C,[43] while for the Y_6WO_{12} compound, the transition from the cubic phase to the hexagonal phase occurred at 1200 °C.[59] Comparatively, the transition temperature of LWO is much lower, and the pure hexagonal phase can be obtained at 1200 °C. This might verify the conclusion drawn by Aitken et al. from another aspect of the crystal.

On the basis of the XRD patterns of LWO:Eu-1300 and LMO:Eu-1300, the lattice constants and atom positions of hexagonal LWO and LMO have been refined by using the Rietveld method on FULLPROF.[60,61] The results are summarized in Tables 1 and 2, and the corresponding refinement profiles are presented in Figure 3. The hexagonal LWO and LMO cells can be described by No.148 space group with R-centered setting. As illustrated in Figure 4, a LWO or LMO cell contains three formula units for a total of 57 atoms. W or Mo atoms occupy 3*a* (0, 0, 0) octahedral sites with six O1 atoms around them, forming $W(Mo)O_6$ octahedra, while Lu atoms occupy 18*f* (*x*, *y*, *z*) sites and have a coordination number of 7, including three O1 atoms and four O2 atoms. The $W(Mo)O_6$ and LuO_7 polyhedra are connected with each other by shearing corners and edges.

The refined lattice constants of LWO and LMO are slightly larger than those reported previously. We ascribe this difference to the doping of Eu^{3+} ions, the ionic radius of which is larger than that of Lu^{3+} ions. In other words, the doping of Eu^{3+} ions increases the ionic radius in 18*f* sites and finally results in the expansion of the lattices. This deduction can be confirmed by the lattice constant variation of isostructural R_6WO_{12} compounds. As reported, the lattice volumes of R_6WO_{12} compounds expand from 732.62 to 766.49 Å^3 and then to 768.12 Å^3 with R changing from Lu to Y and then to Ho, respectively.[53] On the other side, in LWO and LMO cells, the ionic radius of W^{6+} (0.60 Å) is larger than that of Mo^{6+} (0.59 Å).[62] As a result, the W−O bond is longer than the Mo−O bond, the WO_6 coordinate sphere is larger than MoO_6, and eventually the lattice constants of LWO are larger than those of LMO. The lattice constants obtained from DFT calculation are also listed in Table 1. It shows that the results obtained from DFT calculation agree well with the experimental values. The cell volumes of LWO and LMO are 774.75 and 747.39 Å^3, respectively, which are larger than the experimental values by 5.6 and 2.0%, respectively.

3.3. Optical Band Gap Energy and Electronic Structure. Figure S2 of the Supporting Information shows the UV−vis DR spectra of LWO:Eu and LMO:Eu calcinated at different temperatures. It is observed that all the powders have strong absorption of near-UV light. With the transition of the structure and the variation of the crystallinity, the absorption edges of the two compounds shift slightly. The LWO:Eu and LMO:Eu series have absorption edges at ∼350 and ∼450 nm, respectively. The absorption is related to the excitation of electrons from host lattices' valence band (VB) to the conduction band (CB). Although an exact discussion of transitions from VB to CB requires calculation of the excited-state electronic structure, the calculated static electronic band, as an approximation, may still provide important information. The calculated band structure shown in Figure 5 revealed that hexagonal LWO and LMO are indirect band gap materials. The calculated indirect band gap (G point → L point shown in Figure 5) energies are 2.12 eV for LWO and 1.84 eV for LMO. According to the orbital population analysis, the tops of the VBs are identically dominated by the 2p orbitals of O atoms, and the CBs are separated into two parts in both compounds. The upper energy parts are contributed mostly by Lu 5d orbitals, and the lower parts in LWO and LMO, which are also the bottom of the CBs, are formed mainly by the W 5d and Mo 4d orbitals, respectively. Therefore, the interband transition might be approximately viewed as one from O 2p to W 5d (Mo 4d) orbitals.

It was reported that the absorption coefficient (α) of a semiconductor oxide and its band gap energy (E_{gap}) are related

Table 1. Cell Constants *a*, *b*, *c* (in angstroms), and *V* (in cubic angstroms) of Several R_6XO_{12} Compounds and Atomic Coordinates (*x*, *y*, *z*) of Compounds Lu_6WO_{12} and Lu_6MoO_{12}

compound	*a*/*x*	*b*/*y*	*c*/*z*	*V*
Lu_6WO_{12}:Eu[a]	9.6215 (1)	9.6215 (1)	9.1486 (1)	733.45 (3)
Lu:Eu	0.1207 (3)	0.4131 (3)	0.0230 (2)	
W	0	0	0	
O1	0.179 (3)	0.034 (3)	0.117 (2)	
O2	0.138 (3)	0.447 (3)	0.269 (2)	
Lu_6MoO_{12}:Eu[a]	9.6129 (1)	9.6129 (1)	9.1512 (1)	732.33 (3)
Lu (Eu)	0.2922(3)	0.4112(3)	0.0244(2)	
Mo	0	0	0	
O1	0.8506(3)	0.0358(3)	0.1146(2)	
O2	0.3019(3)	0.4451(3)	0.2680(3)	
Lu_6WO_{12}[b]	9.8010	9.8010	9.3130	774.75
Lu	0.2922	0.4112	0.0244	
W	0	0	0	
O1	0.8506	0.0358	0.1146	
O2	0.3019	0.4451	0.2680	
Lu_6MoO_{12}[b]	9.6863	9.6863	9.1981	747.39
Lu	0.2897	0.4089	0.0235	
Mo	0	0	0	
O1	0.8554	0.0384	0.1132	
O2	0.3006	0.4450	0.2681	
Lu_6WO_{12}[c]	9.618	9.618	9.145	732.63
Lu_6MoO_{12}[c]	9.609	9.609	9.147	731.42
Y_6WO_{12}[d]	9.7505	9.7505	9.3094	766.49
Ho_6WO_{12}[d]	9.7583	9.7583	9.3142	768.12

[a]Data determined from powder XRD data by using the Rietveld refinement. Both compounds crystallize in No.148 space group ($R\bar{3}$) within a hexagonal symmetry. $Z = 3$. $\alpha = \beta = 90$. $\gamma = 120$. The reliability factors of the refinement are as follows: for Lu_6WO_{12}:Eu, $R_p = 14.4\%$, $R_{wp} = 20.2\%$, and $\chi^2 = 4.41$, and for Lu_6MoO_{12}:Eu, $R_p = 14.7\%$, $R_{wp} = 20.8\%$, and $\chi^2 = 4.65$. [b]Data obtained from DFT calculation. [c]Experimental data reported by Aitken et al.[30] [d]Experimental data reported by Diot et al.[53]

Table 2. Bond Lengths (in angstroms) of Several R_6XO_{12} (R = Lu, Y, Ho; X = Mo, W) Compounds

	Lu_6WO_{12}[a]	Lu_6MoO_{12}[a]	Lu_6WO_{12}[b]	Lu_6MoO_{12}[b]	Y_6WO_{12}[c]	Ho_6WO_{12}[c]
X−O(1)	1.9119	1.8903	1.9796	1.9251	1.98	1.92
R−O(1)	2.2947	2.3174	2.3600	2.3481	2.46	2.47
R−O(1)	2.4020	2.4236	2.3874	2.3784	2.290	2.359
R−O(1)	2.7009	2.6700	2.7078	2.6394	2.70	2.68
R−O(2)	2.0923	2.1289	2.1934	2.1720	2.277	2.293
R−O(2)	2.1920	2.1655	2.2341	2.2156	2.26	2.22
R−O(2)	2.2682	2.2490	2.2650	2.2500	2.24	2.28
R−O(2)	2.2719	2.2657	2.2880	2.2710	2.19	2.18
R−O	2.3174	2.3172	2.3480	2.3247	2.345	2.354

[a]Data determined from powder XRD data by using Rietveld refinement. [b]Data obtained from DFT calculation. [c]Experimental data reported by Diot et al.[53]

through the following equation:[63]

$$\alpha h\upsilon \propto (h\upsilon - E_{gap})^n \quad (1)$$

where h is Planck's constant, ν is the frequency of the light, and n is a constant depending on the transition type, which can be $^1/_2$, $^3/_2$, or 2 corresponding to direct allowed, direct forbidden, or indirect transition, respectively. In our cases, LWO and LMO have been confirmed to be indirect materials; thus, $n = 2$. According to the Kubelka−Munk equation[64]

$$F(R_\infty) = (1 - R_\infty)^2/2R_\infty = k/s \quad (2)$$

where R_∞ is the diffuse reflectance of the layer relative to the standard, k is the molar absorption coefficient of the sample, and s is the scattering coefficient. Function $F(R_\infty)$ can be obtained from the DR spectra shown in Figure 6a. For a given material, s is independent of the wavelength of the incident light, and k is proportional to the α in eq 1. As a result, $F(R_\infty)$ is proportional to the absorption coefficient α; substituting α with $F(R_\infty)$ in eq 1, we obtain

$$h\upsilon F(R_\infty) \propto (h\upsilon - E_{gap})^2 \quad (3)$$

By plotting $[h\upsilon F(R_\infty)]^{1/2} \sim h\upsilon$ in panels b and c of Figure 6, we determined the band gap energies of LWO and LMO to be 3.02 and 2.61 eV, respectively, which are larger than the DFT-predicted values by 0.8 eV. The inconsistency comes mainly from the use of an unmodified exchange correlation function, which usually underestimates the band gap of semiconductors and insulates, and slightly from the errors introduced from the measurement of the DR spectrum and the estimation by using eqs 1−3.

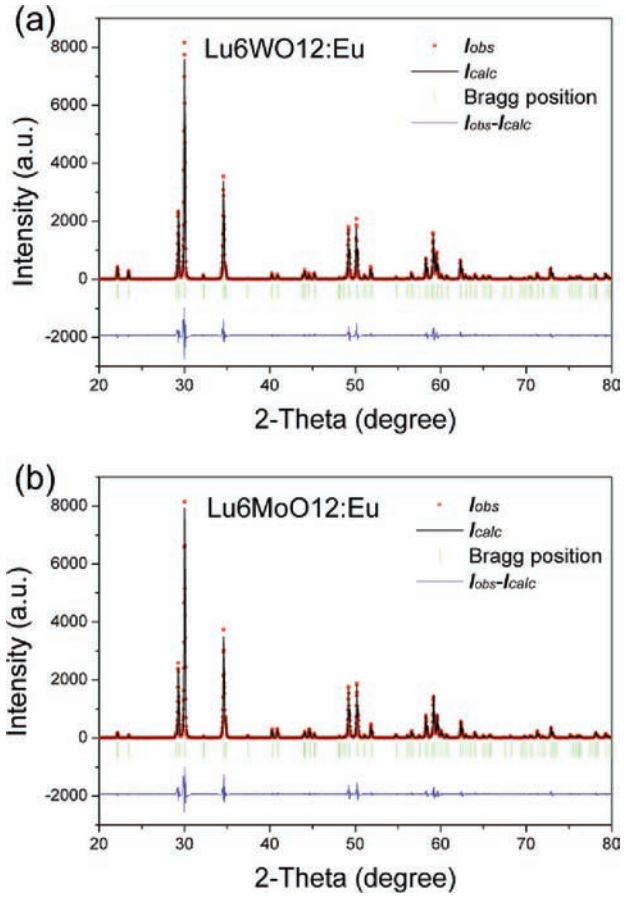

Figure 3. Final Rietveld refinement profiles of (a) LWO:Eu and (b) LMO:Eu. The red dots present the observed data, the black lines through which are the calculated patterns, and the differences between observed and calculated data are plotted at the bottom. The vertical lines indicate the calculated Bragg reflection positions.

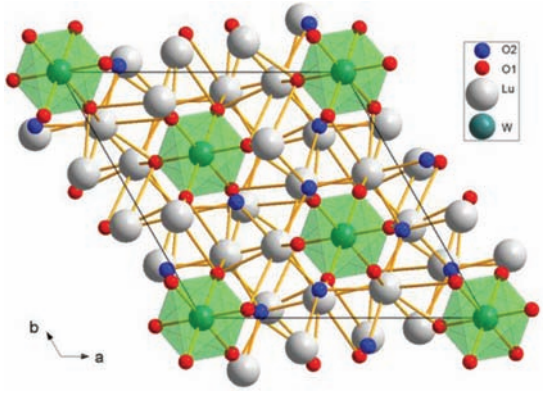

Figure 4. Hexagonal cell of LWO, as well as the coordination of W (green) in the cell.

3.4. Energy Transfer and Photoluminescence Properties. The PL excitation and emission spectra of Eu^{3+} ion-activated LWO and LMO are shown in Figures S3 and S4 of the Supporting Information. Corresponding to two kinds of structures, the spectra of LWO:Eu and LMO:Eu within hexagonal and cubic phases also show two distinct characteristics. We take the samples calcined at 900 and 1300 °C as examples of the cubic and hexagonal phases, respectively, to discuss the structure–property relationship and the energy

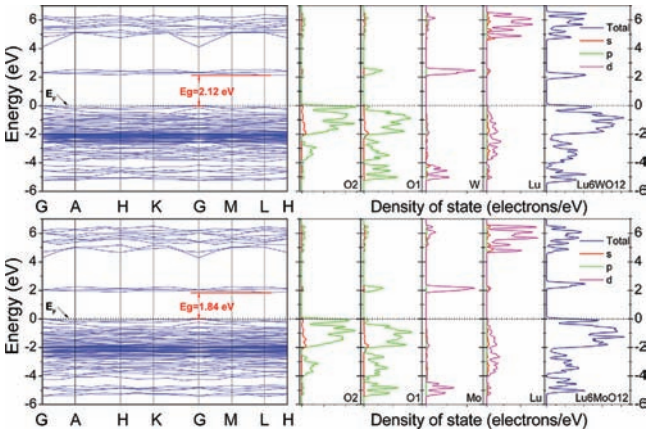

Figure 5. Calculated band structures (left) and orbital populations (right) of hexagonal LWO and LMO near the Fermi energy (E_F) level. The Fermi energy is the zero of the energy scale. Indirect band gap energies from the G point to the L point of LWO and LMO are predicted to be 2.12 and 1.84 eV, respectively.

transfer mechanics from the host lattices to the dopant Eu^{3+} ions.

The PL excitation and emission spectra of LWO and LMO calcined at 900 and 1300 °C are shown in Figure 7. The observed emissions were ascribed to the transitions of Eu^{3+} ion 4f electrons from the $^5D_0$ excited state to ^7F_J (J = 0–4) ground states, e.g., $^5D_0 \rightarrow {}^7F_0$ (578.5 nm of the hexagonal phase, or 580.5 nm of the cubic phase), $^5D_0 \rightarrow {}^7F_1$ (582–605 nm), $^5D_0 \rightarrow {}^7F_2$ (605–640 nm), $^5D_0 \rightarrow {}^7F_3$ (640–670 nm), and $^5D_0 \rightarrow {}^7F_4$ (680–700 nm). With regard to the cubic phase (see Figure 7b,d), the $^5D_0 \rightarrow {}^7F_2$ emission is dominant, while for the hexagonal phase (Figure 7a,c), both $^5D_0 \rightarrow {}^7F_2$ and $^5D_0 \rightarrow {}^7F_1$ emissions are intensive but the $^5D_0 \rightarrow {}^7F_2$ emission is superior.

As is well-known, the $^5D_0 \rightarrow {}^7F_J$ emissions of Eu^{3+} ions are sensitive to site symmetry. If Eu^{3+} ions occupy a site with symmetric inversion, then the $^5D_0 \rightarrow {}^7F_1$ magnetic dipole transitions will dominate and show orange luminescence; otherwise, the $^5D_0 \rightarrow {}^7F_2$ electric dipole transitions will be predominant and show red luminescence. Eu^{3+} ions are therefore a promising structural probe as well as one of the most widely used red light-emitting activators. In our case, there are two kinds of cation sites, namely, W^{6+}/Mo^{6+} and Lu^{3+}. The octahedrally coordinated W^{6+} and Mo^{6+} ions have ionic radii of 0.60 and 0.59 Å, respectively, and the 7-fold coordinated Lu^{3+} ions have an ionic radius of 0.86 Å.[62] Eu^{3+} ions have ionic radii of 0.89 and 0.95 Å in 6- and 7-fold coordination environments, respectively.[62] According to the requirement of charge balance and radius match, Eu^{3+} ions are expected to occupy Lu^{3+} sites. This can be confirmed by the spectral features. In the hexagonal phase, W^{6+} (Mo^{6+}) ions take the 3*a* sites with S_6 point symmetry, while Lu^{3+} ions occupy the 18*f* sites with C_1 symmetry. If Eu^{3+} ions reside in the W^{6+} (Mo^{6+}) sites, only $^5D_0 \rightarrow {}^7F_1$ emissions can be observed; on the other hand, if Eu^{3+} ions move into the Lu^{3+} sites, there will be one, three, and five $^5D_0 \rightarrow {}^7F_0$, $^5D_0 \rightarrow {}^7F_1$, and $^5D_0 \rightarrow {}^7F_2$ emission peaks at most, respectively, within which the $^5D_0 \rightarrow {}^7F_2$ transitions are predominant. The observed spectra are consistent with C_1 symmetry. With regard to the cubic phase, the spectra suggest that the symmetry of the occupied Eu^{3+} ion sites derives further from inversion. This might due to the disordered arrangement of the ions.

dx.doi.org/10.1021/ic201452c | Inorg. Chem. 2011, 50, 12522–12530

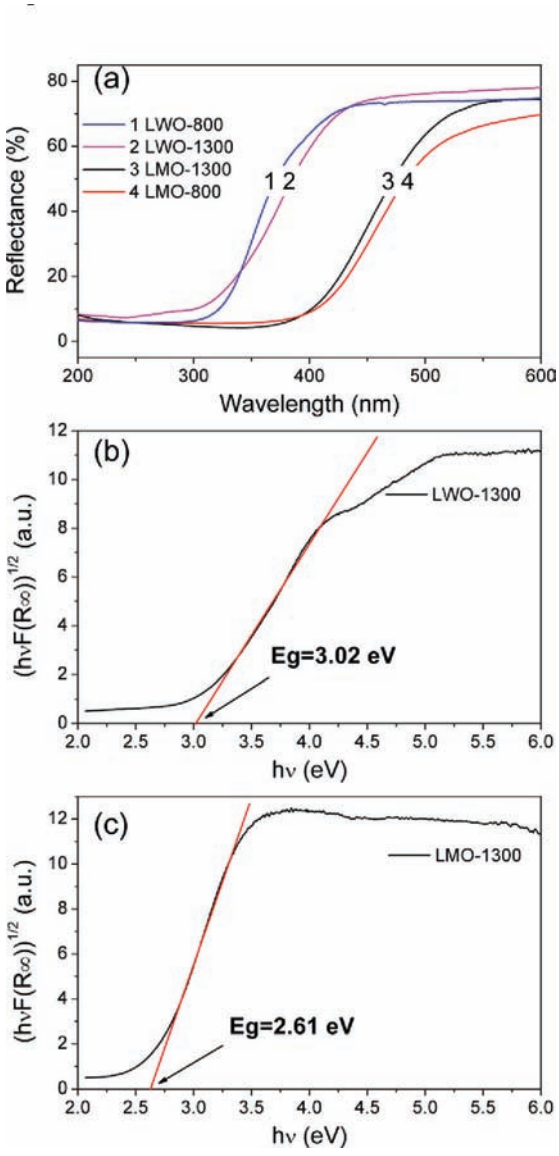

Figure 6. (a) Diffuse reflectance spectra of LWO:Eu-*T* and LMO:Eu-*T* powders calcined at different temperatures *T*. (b and c) Determination of the band gap energies of LWO-1300 (b) and LMO-1300 (c).

It was also observed in Figure 7 that the $^5D_0 \rightarrow {}^7F_0$ peak shifts from 578.5 to 580.5 nm when the compounds transform from the hexagonal phase to the cubic phase, which suggests that the crystal field strength of the environment of Eu^{3+} ions in the hexagonal phase is stronger than that in the cubic phase. This is because a variation in the crystal field can produce a series of modifications in the observed $^5D_0 \rightarrow {}^7F_J$ transitions. One of them is the splitting of the ^7F_J states and the shift of their energy levels. Because both $^5D_0$ and $^7F_0$ states are energetically nondegenerate and cannot be split into sublevels by the crystal field, the $^5D_0 \rightarrow {}^7F_0$ transition of Eu^{3+} ions always consists of a single peak; consequently, the $^5D_0 \rightarrow {}^7F_0$ peak shift is directly related to the crystal field variation.[65−67]

The excitation spectra shown on the left in Figure 7 were collected by monitoring $^5D_0 \rightarrow {}^7F_1$ or $^5D_0 \rightarrow {}^7F_2$ emission of Eu^{3+} ions. It reveals that except for the characteristic excitation of Eu^{3+} ions, such as $^7F_0 \rightarrow {}^5L_6$ and $^7F_0 \rightarrow {}^5D_2$ transitions, there are also broad band centered at 314, 334, 405, and 338 nm for

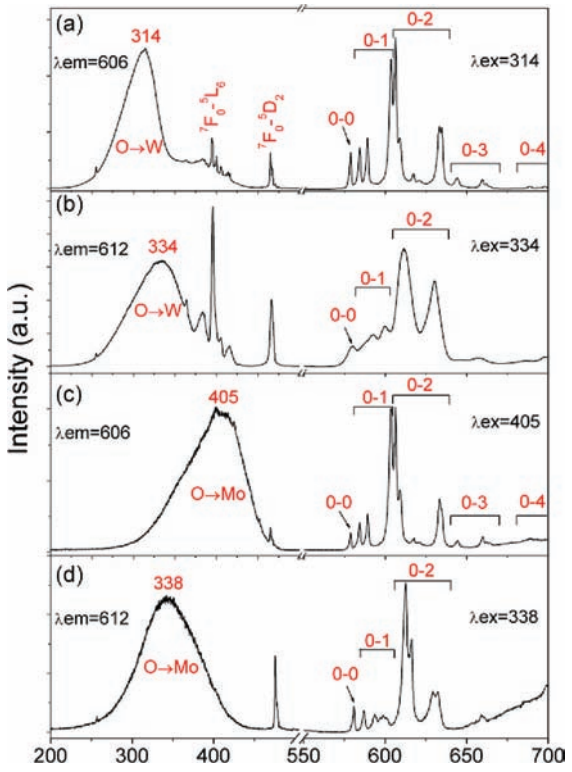

Figure 7. PL excitation and emission spectra of LWO:Eu and LMO:Eu: (a) LWO:Eu-1300, (b) LWO:Eu-900, (c) LMO:Eu-1300, and (d) LMO:Eu-900. 0−*J* (*J* = 0, 1, 2, 3, or 4) stands for the $^5D_0 \rightarrow {}^7F_J$ transitions within Eu^{3+} ion f−f energy levels.

LWO:Eu-1300, LWO:Eu-900, LMO:Eu-1300, and LMO:Eu-900, respectively. According to the DR spectra and the calculated band structures, we know that these bands are excitations of the host lattices, which relate to the electronic transitions from O 2p orbitals to W 5d and Mo 4d orbitals. For all the samples, no emission of the host lattices was observed. This suggests that there is energy transferred from LWO and LMO host lattices to dopant Eu^{3+} ions, and correspondingly, there is energy immigration in the host lattices, which competes against the energy transfer process. From the relative intensity (see Figures S3 and S4 of the Supporting Information), it can be concluded that the efficiency of the transfer of energy from the LWO lattice to Eu^{3+} ions is higher than the efficiency of that from the LMO lattice to Eu^{3+} ions, and the hexagonal phase benefits from the transfer of energy from lattices to Eu^{3+} ions.

One may notice in Figure 7 that the excitation bands of LWO:Eu-900, LWO:Eu-1300, and LMO:Eu-1300 are consistent with the absorption edges in the DR spectra, but the excitation band of LMO:Eu-900 shifts obviously in the high-energy direction relative to the absorption edge in the DR spectrum. As a matter of fact, this phenomenon also exists in other cubic LMO:Eu compounds. We know that the absorption and excitation spectra are closely related but not identical with each other. An absorption spectrum characterizes the interaction between the incident light and a material (including the host lattice and all species within it). An excitation spectrum, however, relates to the absorbed light that can finally result in light emission at the monitor wavelength. If all the light absorbed can be equally converted into emission light, the absorption spectrum and the excitation spectrum should be

identical, but this situation is ideal. In a real phosphor, especially the emission is realized by means of the transfer of energy between the host lattice and dopant, such as the underconsidered LWO:Eu and LMO:Eu systems, some of the absorbed energy might finally arrive at dopant Eu^{3+} and luminesce, while the others might be trapped by defects or converted into phonon emission. Both of these parts are shown in the absorption spectrum, but only the former is shown in the excitation spectrum. As mentioned earlier, the cubic LMO:Eu is in a defect fluorite structure and not well crystallized. As a result, there are a great amount of defects, which might trap the energy within the range of 375−450 nm, and this finally leads to the divergence between the excitation and absorption spectra.

We also checked the PL decay property of all the phosphors by exciting the host lattices and observing the emission of Eu^{3+} ions. The decay data of LWO:Eu-1300, LWO:Eu-900, LMO:Eu-1300, and LMO:Eu-900 samples are representatively depicted in Figure 8. The decay data of other samples are

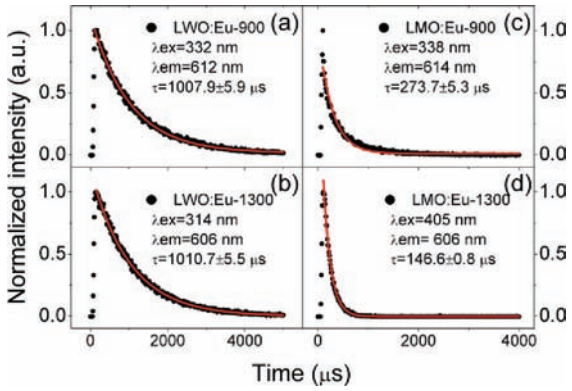

Figure 8. Temporal decay data of LWO:Eu and LMO:Eu: (a) LWO:Eu-900, (b) LWO:Eu-1300, (c) LMO:Eu-900, and (d) LMO:Eu-1300.

shown in Figures S5 and S6 of the Supporting Information. As observed in the figures, all the luminescence decay data can be fitted to a single-exponential function

$$I_t = I_0 \exp(-t/\tau) \tag{4}$$

where I_t and I_0 are the intensity at time t and time zero, respectively, and τ is the lifetime. The determined luminescence lifetimes of the LWO:Eu and LMO:Eu series are plotted in Figure 9. Although the structure and luminescence of the LWO:Eu and LMO:Eu series evolve in similar patterns, there are significant differences in the decay property. First, the lifetimes of the LWO:Eu series are longer than those of the LMO:Eu series. Second, the lifetime of the LWO:Eu series is almost kept consistent (within a range of 988−1053 μs) and independent of the calcination temperature. On the other hand, the lifetime of the LMO:Eu series decreases gradually from 383 μs for LMO:Eu-800 to 147 μs for LMO:Eu-1300. The experimentally determined lifetime contains both radiative and nonradiative contributions, namely

$$\frac{1}{\tau} = \sum_i (A_i + W_i) = \sum_i \left(\frac{1}{\tau_i} + W\right) \tag{5}$$

where τ is the experimental lifetime determined by eq 4, A_i and W_i are radiative and nonradiative transition probabilities,

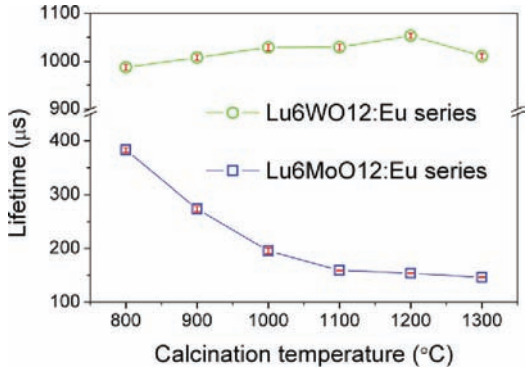

Figure 9. Variation in the PL decay lifetime of LWO:Eu and LMO:Eu with calcination temperature.

respectively, τ_i is the radiative lifetime of an energy pair, and i indicates transitions from the excited energy level to all possible levels below. Consequently, the change in both the radiative process and the nonradiative process affects the experimental result. In our cases, with the transition of the structure from the cubic phase to the hexagonal phase, the luminescence intensity increases, indicating the reduced nonradiative process (decrease in W_i) and enhanced radiative process (increase in A_i). The possible reason for the evolution of the decay lifetime might be the balance of W_i and A_i: for the LWO:Eu series, the effect is counteracted, while for the LMO:Eu series, the increase in A_i is over the decrease in W_i.

In recent decades, because of the rapid development of LED technology and the requirement of energy saving and environmental protection, near-UV LED-based solid-state lighting has been investigated widely and intensively.[68−71] As one of the most important components, near-UV LED-based color-conversion phosphors were also extensively researched.[70,71] As a color-conversion phosphor for near-UV-based LED, it is expected to absorb near-UV light efficiently and convert the excitation energy into red, green, or blue light emission.[70,71] Eu^{3+} ion-activated molybdates and tungstates were widely suggested to be red phosphors for near-UV LED. According to the structure of the host lattice, the suggested phosphors can be roughly divided into two groups. Within one of the groups, the host lattices contain 4-fold coordinated W/Mo, namely WO_4/MoO_4 groups.[2−13,72] In the other group, the coordination number of W/Mo is higher, which might be 5 or 6.[47,48,73−80] It was reported that the position of the excitation band of MoO_x groups depends on the coordination number x.[81] Generally, an increase in x results in the excitation band shifting in the long-wavelength direction. A similar phenomenon has also been observed in the tungstates. The different structural features of the two groups determine the divergence of the excitation patterns. Compounds containing WO_4/MoO_4 complexes are usually excited directly into Eu^{3+} f−f transition because of the host lattice excitation band located at a high-energy position, and therefore, near-UV light cannot be efficiently absorbed by host lattices. For compounds having high-fold coordinated W/Mo, energy within the near-UV region can be efficiently absorbed and transferred to dopant Eu^{3+} ions; the energy transfer channel is usually used to excite Eu^{3+} ions. Compounds LWO and LMO reported here belong to the second group, containing 6-fold coordinated W/Mo. The optical and photoluminescence spectra shown in Figures 6 and 7 indicate that LWO:Eu and LMO:Eu show excellent near-UV absorption characteristic, and under near-UV excitation, the

dx.doi.org/10.1021/ic201452c | Inorg. Chem. 2011, 50, 12522−12530

compounds show intensive red luminescence. Therefore, these compounds are suggested as candidates for the red color-conversion phosphor for solid-state lighting.

4. CONCLUSIONS

(1) Polycrystalline LWO:Eu and LMO:Eu have been synthesized by using a citrate complexation method. Both cubic and hexagonal phases have been obtained. (2) The lattice constants of hexagonal LWO and LMO have been determined. (3) LWO and LMO show strong absorption of near-UV light, which was ascribed to the interband transition from O 2p orbitals to W 5d and Mo 4d orbitals within WO_6 and MoO_6 groups. The band gap energies of the hexagonal Lu_6WO_{12} and Lu_6MoO_{12} have been determined from the diffuse reflectance spectra. (4) Upon near-UV excitation, both LWO:Eu and LMO:Eu series show intensive red luminescence because of the transfer of energy from WO_6 and MoO_6 groups to dopant Eu^{3+} ions. The energy transfer efficiency of the $WO_6 \rightarrow Eu^{3+}$ transition is higher than that of the $MoO_6 \rightarrow Eu^{3+}$ transition. On the other hand, the hexagonal phase benefits the transfer of energy in both compounds. These compounds were suggested to be red color-conversion phosphors for WLED devices because of their color-conversion property from near-UV to red.

■ ASSOCIATED CONTENT

Supporting Information

SEM microimages and EDX data of LWO:Eu samples calcined at different temperatures, figures of diffuse reflectance, photoluminescence excitation, and emission spectra, and temporal decay data of LWO:Eu and LMO:Eu samples calcined at different temperatures. This material is available free of charge via the Internet at http://pubs.acs.org.

■ AUTHOR INFORMATION

Corresponding Author

*E-mail: jhjeong@pknu.ac.kr. Fax: +82-51-629-5549. Telephone: +82-51-629-5564.

■ ACKNOWLEDGMENTS

This study was supported by a Korea Research Foundation Grant funded by the Korean Government (NRF-2010-0029634), by the Industrial Strategic Technology Development Program (Project 10037416) funded by the Ministry of Knowledge Economy (MKE, Korea), and also partially by the National Core Research Center Program through the NRF of Korea funded by the Ministry of Education, Science and Technology (2010-0001-226).

■ REFERENCES

(1) Yen, W. M.; Weber, M. J. *Inorganic Phosphors: Compositions, Preparation and Optical Properties*; CRC Press: Boca Raton, FL, 2004.
(2) Xu, Z.; Li, C.; Li, G.; Chai, R.; Peng, C.; Yang, D.; Lin, J. *J. Phys. Chem. C* **2010**, *114*, 2573−2582.
(3) Esteban-Betegón, F. t.; Zaldo, C.; Cascales, C. n. *Chem. Mater.* **2010**, *22*, 2315−2324.
(4) Dong, F.; Huang, Y.; Zou, S.; Liu, J.; Lee, S. C. *J. Phys. Chem. C* **2011**, *115*, 241−247.
(5) Zhang, F.; Wong, S. S. *ACS Nano* **2010**, *4*, 99−112.
(6) Lei, F.; Yan, B.; Chen, H.-H.; Zhang, Q.; Zhao, J.-T. *Cryst. Growth Des.* **2009**, *9*, 3730−3736.
(7) Lei, F.; Yan, B.; Chen, H. H.; Zhao, J. T. *Inorg. Chem.* **2009**, *48*, 7576−7584.
(8) Li, Y.-Y.; Cheng, W.-D.; Zhang, H.; Lin, C.-S.; Zhang, W.-L.; Geng, L.; Chai, G.-L.; Luo, Z.-Z.; He, Z.-Z. *Dalton Trans.* **2011**, *40*, 7357−7364.
(9) Ding, Y.; Wan, Y.; Min, Y.-L.; Zhang, W.; Yu, S.-H. *Inorg. Chem.* **2008**, *47*, 7813−7823.
(10) Marques, V. S.; Cavalcante, L. S.; Sczancoski, J. C.; Alcantara, A. F. P.; Orlandi, M. O.; Moraes, E.; Longo, E.; Varela, J. A.; Siu Li, M.; Santos, M. R. M. C. *Cryst. Growth Des.* **2010**, *10*, 4752−4768.
(11) Sczancoski, J. C.; Bomio, M. D. R.; Cavalcante, L. S.; Joya, M. R.; Pizani, P. S.; Varela, J. A.; Longo, E.; Li, M. S.; Andrés, J. A. *J. Phys. Chem. C* **2009**, *113*, 5812−5822.
(12) Cavalcante, L. S.; Sczancoski, J. C.; Lima, L. F.; Espinosa, J. W. M.; Pizani, P. S.; Varela, J. A.; Longo, E. *Cryst. Growth Des.* **2009**, *9*, 1002−1012.
(13) Cavalli, E.; Boutinaud, P.; Mahiou, R.; Bettinelli, M.; Dorenbos, P. *Inorg. Chem.* **2010**, *49*, 4916−4921.
(14) Amano, F.; Yamakata, A.; Nogami, K.; Osawa, M.; Ohtani, B. *J. Am. Chem. Soc.* **2008**, *130*, 17650−17651.
(15) Zhou, L.; Yu, M.; Yang, J.; Wang, Y.; Yu, C. *J. Phys. Chem. C* **2010**, *114*, 18812−18818.
(16) Chen, X.; Shen, S.; Guo, L.; Mao, S. S. *Chem. Rev.* **2010**, *110*, 6503−6570.
(17) Zhang, L.; Man, Y.; Zhu, Y. *ACS Catal.* **2011**, *1*, 841−848.
(18) Zhang, C.; Zhu, Y. *Chem. Mater.* **2005**, *17*, 3537−3545.
(19) Lin, J.; Lin, J.; Zhu, Y. *Inorg. Chem.* **2007**, *46*, 8372−8378.
(20) Liu, S.-S.; Yang, D.-P.; Ma, D.-K.; Wang, S.; Tang, T.-D.; Huang, S.-M. *Chem. Commun.* **2011**, *47*, 8013−8015.
(21) Kongmark, C.; Martis, V.; Rubbens, A.; Pirovano, C.; Lofberg, A.; Sankar, G.; Bordes-Richard, E.; Vannier, R.-N.; Van Beek, W. *Chem. Commun.*, **2009**, 4850−4852.
(22) Kudo, A.; Miseki, Y. *Chem. Soc. Rev.* **2009**, *38*, 253−278.
(23) Yourey, J. E.; Bartlett, B. M. *J. Mater. Chem.* **2011**, *21*, 7651−7660.
(24) Lacorre, P.; Goutenoire, F.; Bohnke, O.; Retoux, R.; Laligant, Y. *Nature* **2000**, *404*, 856−858.
(25) Imanaka, N.; Ueda, T.; Okazaki, Y.; Tamura, S.; Adachi, G.-y. *Chem. Mater.* **2000**, *12*, 1910−1913.
(26) Goutenoire, F.; Isnard, O.; Retoux, R. *Chem. Mater.* **2000**, *12*, 2575−2580.
(27) Evans, I. R.; Howard, J. A. K.; Evans, J. S. O. *Chem. Mater.* **2005**, *17*, 4074−4077.
(28) Orera, A.; Slater, P. R. *Chem. Mater.* **2010**, *22*, 675−690.
(29) Malavasi, L.; Kim, H.; Billinge, S. J. L.; Proffen, T.; Tealdi, C.; Flor, G. *J. Am. Chem. Soc.* **2007**, *129*, 6903−6907.
(30) Aitken, E. A.; Bartram, S. F.; Juenke, E. F. *Inorg. Chem.* **1964**, *3*, 949−954.
(31) Yoshimura, M.; Sibieude, F.; Rouanet, A.; Foex, M. *J. Solid State Chem.* **1976**, *16*, 219−232.
(32) Chang, L. L. Y.; Phillips, B. *Inorg. Chem.* **1964**, *3*, 1792−1794.
(33) McCarthy, G. J.; Fischer, R. D.; Johnson, G. J.; Goode, C. E. *NBS Spec. Publ. (U.S.)* **1972**, *364*, 397.
(34) Trunov, V. K.; Tyushevskaya, G. I.; Afonskii, N. S. *Russ. J. Inorg. Chem.* **1968**, *13*, 491−493.
(35) McCarthy, G. J. *Mater. Res. Bull.* **1971**, *6*, 31−39.
(36) Borchardt, H. J. *Inorg. Chem.* **1963**, *2*, 170−173.
(37) Kuribayashi, K.; Yoshimura, M.; Ohta, T.; Sata, T. *J. Am. Ceram. Soc.* **1980**, *63*, 644−647.
(38) Magrasó, A.; Frontera, C.; Marrero-López, D.; Núñez, P. *Dalton Trans.*, **2009**, 10273−10283.
(39) Yoshimura, M.; Baumard, J. F. *Mater. Res. Bull.* **1975**, *10*, 983−988.
(40) Shimura, T.; Fujimoto, S.; Iwahara, H. *Solid State Ionics* **2001**, *143*, 117−123.
(41) Haugsrud, R. *Solid State Ionics* **2007**, *178*, 555−560.
(42) Haugsrud, R.; Kjølseth, C. *J. Phys. Chem. Solids* **2008**, *69*, 1758−1765.
(43) Escolástico, S.; Vert, V. B.; Serra, J. M. *Chem. Mater.* **2009**, *21*, 3079−3089.

(44) Solís, C.; Escolastico, S.; Haugsrud, R.; Serra, J. M. *J. Phys. Chem. C* **2011**, *115*, 11124−11131.
(45) Haugsrud, R.; Fjeld, H.; Haug, K. R.; Norby, T. *J. Electrochem. Soc.* **2007**, *154*, B77−B81.
(46) Beaury, O.; Faucher, M.; Caro, P. *Mater. Res. Bull.* **1978**, *13*, 175−185.
(47) Zheng, Y.; You, H.; Liu, K.; Song, Y.; Jia, G.; Huang, Y.; Yang, M.; Zhang, L.; Ning, G. *CrystEngComm* **2011**, *13*, 3001−3007.
(48) Li, H.; Yang, H. K.; Moon, B. K.; Choi, B. C.; Jeong, J. H.; Jang, K.; Lee, H. S.; Yi, S. S. *J. Mater. Chem.* **2011**, *21*, 4531−4537.
(49) Tian, Y.; Chen, B.; Hua, R.; Zhong, H.; Cheng, L.; Sun, J.; Lu, W.; Wan, J. *Physica B* **2009**, *404*, 3598−3601.
(50) Yu, T.; Sun, J.; Hua, R.; Cheng, L.; Zhong, H.; Li, X.; Yu, H.; Chen, B. *J. Alloys Compd.* **2011**, *509*, 391−395.
(51) Cheviré, F.; Clabau, F.; Larcher, O.; Orhan, E.; Tessier, F.; Marchand, R. *Solid State Sci.* **2009**, *11*, 533−536.
(52) Cheviré, F.; Muñoz, F.; Baker, C. F.; Tessier, F.; Larcher, O.; Boujday, S.; Colbeau-Justin, C.; Marchand, R. *J. Solid State Chem.* **2006**, *179*, 3184−3190.
(53) Diot, N.; Benard-Rocherulle, P.; Marchand, R. *Powder Diffr.* **2000**, *15*, 220−226.
(54) Segall, M. D.; Philip, J. D. L.; Probert, M. J.; Pickard, C. J.; Hasnip, P. J.; Clark, S. J.; Payne, M. C. *J. Phys.: Condens. Matter* **2002**, *14*, 2717.
(55) Vanderbilt, D. *Phys. Rev. B* **1990**, *41*, 7892.
(56) Monkhorst, H. J.; Pack, J. D. *Phys. Rev. B* **1976**, *13*, 5188.
(57) Ceperley, D. M.; Alder, B. J. *Phys. Rev. Lett.* **1980**, *45*, 566.
(58) Perdew, J. P.; Zunger, A. *Phys. Rev. B* **1981**, *23*, 5048.
(59) Yoshimura, M.; Ma, J.; Kakihana, M. *J. Am. Ceram. Soc.* **1998**, *81*, 2721−2724.
(60) Rodriguez-Carvajal, J. *FullProf 2000: A Rietveld Refinement and Pattern Matching Analysis Program* (accessed April 2008). http://www.ill.eu/sites/fulprof/.
(61) Roisnel, J.; Rodríguez-Carvajal, J. *WINPLOTR: a Windows tool for powder diffraction patterns analysis Materials Science Forum*. Proceedings of the Seventh European Powder Diffraction Conference (EPDIC 7), 2000; p 118.
(62) Shannon, R. *Acta Crystallogr.* **1976**, *A32*, 751−767.
(63) Wood, D. L.; Tauc, J. *Phys. Rev. B* **1972**, *5*, 3144.
(64) Tandon, S. P.; Gupta, J. P. *Phys. Status Solidi B* **1970**, *38*, 363−367.
(65) Albin, M.; Horrocks, W. D. *Inorg. Chem.* **1985**, *24*, 895−900.
(66) Frey, S. T.; Horrocks, W. D. *Inorg. Chim. Acta* **1995**, *229*, 383−390.
(67) Choppin, G. R.; Wang, Z. M. *Inorg. Chem.* **1997**, *36*, 249−252.
(68) Schubert, E. F.; Kim, J. K. *Science* **2005**, *308*, 1274−1278.
(69) Fred Schubert, E. *Light-Emitting Diodes*; Cambridge University Press: Cambridge, U.K., 2003.
(70) Justel, T. Luminescent Materials for Phosphor-Converted LEDs. In *Luminescence: From Theory to Applications*; Ronda, C., Ed.; Wiley-VCH Verlag GmbH & Co. KGaA: Weinheim, Germany, 2008; pp 179−190.
(71) Silver, J.; Withnall, R. Color Conversion Phosphors for LEDS. In *Luminescent Materials and Applications*; Kitai, A., Ed.; John Wiley & Sons, Ltd.: Chichester, U.K., 2008; pp 75−109.
(72) Lei, F.; Yan, B.; Chen, H.-H. *J. Solid State Chem.* **2008**, *181*, 2845−2851.
(73) Li, H.; Yang, H. K.; Jeong, J. H.; Jang, K.; Lee, H. S.; Yi, S. S. *Mater. Res. Bull.* **2011**, *46*, 1352−1358.
(74) Li, H.; Yang, H. K.; Moon, B. K.; Choi, B. C.; Jeong, J. H.; Jang, K.; Lee, H. S.; Yi, S. S. *J. Alloys Compd.* **2011**, *509*, 8788−8793.
(75) Li, H.; Zhang, S.; Zhou, S.; Cao, X.; Zheng, Y. *J. Phys. Chem. C* **2009**, *113*, 13115−13120.
(76) Sivakumar, V.; Varadaraju, U. V. *Electrochem. Solid-State Lett.* **2006**, *9*, H35−H38.
(77) Sivakumar, V.; Varadaraju, U. V. *J. Electrochem. Soc.* **2007**, *154*, J28−J31.
(78) Sivakumar, V.; Varadaraju, U. V. *J. Solid State Chem.* **2008**, *181*, 3344−3351.
(79) Ye, S.; Wang, C. H.; Liu, Z. S.; Lu, J.; Jing, X. P. *Appl. Phys. B: Lasers Opt.* **2008**, *91*, 551−557.
(80) Ye, S.; Wang, C. H.; Jing, X. P. *J. Electrochem. Soc.* **2008**, *155*, J148−J151.
(81) Wiegel, M.; Blasse, G. *J. Solid State Chem.* **1992**, *99*, 388−394.